Energy & Environmental Science

Origins of hydrogen peroxide selectivity during oxygen reduction on organic mixed ionic-electronic conducting polymers

Journal:	*Energy & Environmental Science*
Manuscript ID	EE-ART-06-2023-002102.R1
Article Type:	Paper
Date Submitted by the Author:	07-Sep-2023
Complete List of Authors:	De La Fuente Durán, Ana; Stanford University, Materials Science & Engineering Liang, Allen; Stanford University, Department of Chemistry Denti, Ilaria; Stanford University, Materials Science & Engineering Yu, Hang; Imperial College London, Physics Pearce, Drew; Imperial College London, Chemistry Marks, Adam; Stanford University, Materials Science & Engineering Penn, Emily; Stanford University, Chemical Engineering Treiber, Jeremy; Stanford University, Materials Science & Engineering Weaver, Karrie; Stanford University, Earth System Science Turaski, Lily; Stanford University, Materials Science & Engineering Maria, Iuliana; Imperial College London, Chemistry; University of Oxford, Chemistry, Chemistry Research Laboratory Griggs, Sophie; University of Oxford, Chen, Xingxing; Anhui University, Department of Materials, School of Chemistry and Chemical Engineering Salleo, Alberto; Stanford University, Materials Science & Engineering Chueh, William; Stanford University, Materials Science & Engineering Nelson, Jenny; Imperial College of Science Technology and Medicine, Physics Giovannitti, Alexander; Stanford University, Materials Science & Engineering; Chalmers University of Technology, Chemistry and Chemical Engineering Mefford, J.; Stanford University, Materials Science & Engineering

Broader context

Oxygen reduction is an important reaction for the transition towards carbon-neutral energy and chemical production as it enables the generation of electricity through electrochemical devices (e.g. fuel cells and metal-air batteries) and the environmentally-benign production of hydrogen peroxide in electrolyzers. Oxygen reduction proceeds through a multi-proton, multi-electron process resulting in slow kinetics that generally require the use of electrocatalysts for efficient operation. While typical electrocatalysts are composed of rare precious metals or transition metal oxides, recent efforts have demonstrated organic materials can act as oxygen reducing electrodes without the use of metals. In this work, we investigate a set of metal-free conjugated polymers as oxygen reduction electrodes to understand the origins of their activity and selectivity. Through both experiment and theory, we provide a framework to understand the oxygen reducing mechanism of this emerging class of materials. Our results show that these polymeric electrodes do indeed reduce oxygen, but not through the common catalytic pathways operative on metal containing electrocatalysts. Importantly, this pathway allows a model n-type semiconducting polymer, p(NDI-T2 P75), to selectively reduce oxygen to hydrogen peroxide at overpotentials < 100 mV in alkaline conditions, demonstrating promising opportunities for polymers as oxygen reducing electrodes.

Origins of hydrogen peroxide selectivity during oxygen reduction on organic mixed ionic-electronic conducting polymers

Ana De La Fuente Durán[1], Allen Yu-Lun Liang[2], Ilaria Denti[1], Hang Yu[3], Drew Pearce[3], Adam Marks[1], Emily Penn[4], Jeremy Treiber[1], Karrie Weaver[5], Lily Turaski[1], Iuliana P. Maria[6,7], Sophie Griggs[7], Xingxing Chen[8], Alberto Salleo[1], William C. Chueh[1], Jenny Nelson[3], Alexander Giovannitti[1,9]*, J. Tyler Mefford[1,*]

1. Department of Materials Science and Engineering, Stanford University, Stanford, CA 94305, USA.

2. Department of Chemistry, Stanford University, Stanford, CA 94305, USA.

3. Department of Physics, Imperial College London, London SW7 2AZ, United Kingdom

4. Department of Chemical Engineering, Stanford University, Stanford, CA 94305, USA.

5. Department of Earth System Science, Stanford University, Stanford, CA 94305, USA.

6. Department of Chemistry, Imperial College London, London W12 0BZ, United Kingdom.

7. Department of Chemistry, Chemistry Research Laboratory, University of Oxford, Oxford OX1 3TA, United Kingdom.

8. Department of Materials, School of Chemistry and Chemical Engineering, Anhui University, Hefei 230601, Anhui, People's Republic of China.

9. Department of Chemistry and Chemical Engineering, Chalmers University of Technology, Gothenburg, 412 96, Sweden.

Abstract

Electrochemical reduction of atmospheric oxygen provides carbon emission-free pathways for the generation of electricity from chemical fuels and for the distributed production of green chemical oxidants like hydrogen peroxide. Recently, organic mixed ionic-electronic conducting polymers (OMIECs) have been reported as a new class of active electrode materials for the oxygen reduction reaction. This work sets out to identify the operative oxygen reduction mechanism of OMIECs through a multi-faceted experimental and theoretical approach. Using a combination of pH-dependent electrochemical characterization, *operando* UV-Vis and Raman spectroscopy, and *ab initio* calculations, we find that the n-type OMIEC, p(NDI-T2 P75), displays pH-dependent activity for the selective reduction of oxygen to the 2-electron hydrogen peroxide product. We use microkinetic simulations of the electrochemical behavior to rationalize our experimental observations through a polaron-mediated, non-adsorptive pathway involving chemical reduction of oxygen to the 1-electron superoxide intermediate followed by pH-dependent catalytic disproportionation to hydrogen peroxide. Finally, this pathway is applied to understand the experimental oxygen reduction reactivity across several n- and p-type OMIECs.

Broader context

Oxygen reduction is an important reaction for the transition towards carbon-neutral energy and chemical production as it enables the generation of electricity through electrochemical devices (e.g. fuel cells and metal-air batteries) and the environmentally-benign production of hydrogen peroxide in electrolyzers. Oxygen reduction proceeds through a multi-proton, multi-electron process resulting in slow kinetics that generally require the use of electrocatalysts for efficient operation. While typical electrocatalysts are composed of rare precious metals or transition metal oxides, recent efforts have demonstrated organic materials can act as oxygen reducing electrodes without the use of metals. In this work, we investigate a set of metal-free conjugated polymers as oxygen reduction electrodes to understand the origins of their activity and selectivity. Through both experiment and theory, we provide a framework to understand the oxygen reducing mechanism of this emerging class of materials. Our results show that these polymeric electrodes do indeed reduce oxygen, but not through the common catalytic pathways operative on metal containing electrocatalysts. Importantly, this pathway allows a model n-type semiconducting polymer, p(NDI-T2 P75), to selectively reduce oxygen to hydrogen peroxide at overpotentials < 100 mV in alkaline conditions, demonstrating promising opportunities for polymers as oxygen reducing electrodes.

Introduction

Mitigating greenhouse gas emissions in the energy and chemical industries requires a transition from current fossil fuel-based thermochemical processes to carbon emission-free electrochemical processes. Given its abundance, atmospheric molecular oxygen is an attractive oxidant for the generation of electricity from chemical fuels (such as H_2 or methanol in fuel cells[1–4] or metals like Zn, Fe, or Al in metal-air batteries[5–8]) or for the distributed on-site electrochemical production of hydrogen peroxide (more details in Supplementary Note 1).[9,10] In aqueous systems at room temperature, these separate applications require different selectivity in the terminal product of oxygen reduction, where generating hydrogen peroxide terminates at a net 2-electron/2-proton reduction (hydrogen peroxide production reaction, HPPR: $O_2 + 2H^+ + 2e^- \rightleftharpoons H_2O_2$, $E^0 = 0.695$ V vs. SHE) and fuel cell or metal-air battery applications ideally reduce oxygen to water through a net 4-electron/4-proton process (oxygen reduction reaction, ORR: $O_2 + 4H^+ + 4e^- \rightleftharpoons 2H_2O$, $E^0 = 1.23$ V vs. SHE).

Although not universal, it is generally assumed that an electrocatalyst is needed to reduce oxygen. Recently, organic mixed ionic-electronic conducting polymers (OMIECs) have been reported to exhibit catalytic behavior for electrochemical reactions.[11–15] OMIECs are semiconducting conjugated polymers with synthetically tunable structures and transport properties enabled by electrochemical ion-insertion redox reactions.[16] These electrochemical "doping" reactions drive the insertion of mobile ions and electrons (or holes), providing

functionality for a range of electrochemical devices.[16–21] For electrocatalysis, hole/anion transporting OMIECs (p-type), including PEDOT (poly(3,4-ethylenedioxythiophene)) variations, have been studied for oxygen reduction and display selectivity for the 2-electron reaction.[13,14,22] BBL (poly(benzimidazobenzophenanthroline)), an electron/cation transporting (n-type) OMIEC, has also been shown to be active for the ORR, with pH-dependent selectivity for the 4-electron versus the 2-electron product.[15] These studies highlight the potential of OMIECs as electrodes for oxygen reduction, but the fundamental design principles that control their activities and selectivity are still being developed.

Our work sets out to identify the operative oxygen reduction mechanism of OMIECs through a multi-faceted experimental and theoretical approach. We focus our efforts on p(NDI-T2 P75), a naphthalene-1,4,5,8-tetracarboxylic-diimide-bithiophene copolymer with 75% polar side chains (Figure 1a).[23] NDI-T2 copolymers are acceptor-donor copolymers which exhibit good charge transport properties relative to other n-type OMIECs. The fraction of polar sidechains in p(NDI-T2 P75) enables its bulk-ion insertion redox in aqueous electrolytes. An NDI-T2 polymer with entirely nonpolar side chains (Figure 1b) fails to exhibit redox behavior when operated in the same electrolyte (Figure 1c). Notably, p(NDI-T2 P75) is stable in a broad pH range, is structurally similar to a previously described oxygen-reducing OMIEC,[24] and has heteroatoms and functional groups reported to be vital for electrocatalysis on carbon-based materials, including N, carbonyl groups (C=O), and S.[25–28]

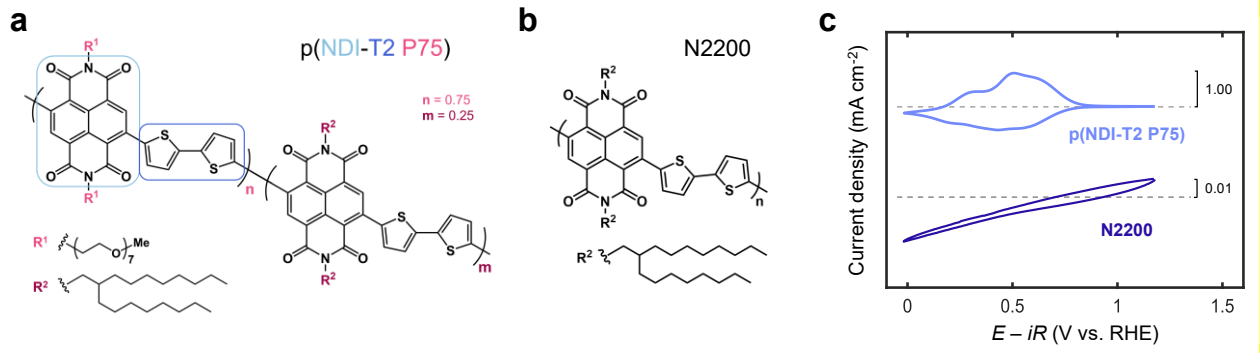

Figure 1. **a)** Structure of p(NDI-T2 P75), an acceptor-donor random copolymer with a backbone composed of an electron-deficient naphthalene diimide (NDI) unit and an electron-rich bithiophene (T2) unit. The hydrophilic side chains based on ethylene glycol, R^1, attached to 75% of monomer units (P75) facilitate solvated ion-insertion, and the hydrophobic side chains based on alkyl chains, R^2, provide improved electrochemical stability.[29] **b)** Structure of N2200, an NDI-T2 polymer with 100% hydrophobic alkyl side chains. **c)** Cyclic voltammograms of p(NDI-T2 P75) and N2200 in Ar-saturated 0.1 M KOH at a scan rate of 5 mV s^{-1}.

We combine rotating ring-disk electrochemistry, *operando* spectroscopy techniques, and *ab initio* and steady-state microkinetic simulations to evaluate the performance and mechanism of p(NDI-T2 P75) for oxygen reduction. We validate the generality of our mechanistic conclusions by benchmarking the performance of an expanded selection of p- and n-type OMIECs. The rigorous approach to studying electrochemical H_2O_2 production presented here is generalizable beyond OMIECs and facilitates a guided exploration to understand the operating principles of oxygen reducing electrodes.

Results and discussion

Understanding the Electrochemistry of p(NDI-T2 P75)

Prior to all electrochemical experiments, p(NDI-T2 P75) was purified to remove residual Pd contamination from polymer synthesis (Figure S1, Table S1), resulting in low Pd concentrations of 2 – 5 ppm. While it has been reported that a polymer much like p(NDI-T2 P75) primarily produces H_2O upon reducing O_2 in a 4-electron reaction,[24] we demonstrate that the removal of residual Pd is crucial for revealing intrinsic electrochemical performance. We find residual Pd impurities result in a positive shift in the measured halfwave voltage, $E_{1/2}$, for oxygen reduction and modifies the selectivity from H_2O_2 towards H_2O as the majority product (Figure S2).[30]

We use rotating ring-disk electrochemistry (RRDE) to investigate the behavior of p(NDI-T2 P75) in $[K^+]$ = 1 M aqueous electrolytes with pH varied between 7.0 and 14.2. Characteristic voltammograms at a scan rate of 5 mV s^{-1} for p(NDI-T2 P75) in Ar-saturated electrolytes are shown in Figure 2a. For all tested pH values, three reversible redox peaks are observed. The first two peaks, which appear at more positive voltages, correspond to electron polaron formation and the third peak corresponds to the formation of the electron bipolaron.[31] We confirm the n-type nature of these electron polaron formation reactions through conductivity measurements using an interdigitated electrode array in an organic electrochemical transistor (OECT) architecture (Figure S3). The formation of the electron polaronic state is associated with electron/cation “doping” of the polymer film resulting in an electronic conductivity enhancement by a factor of $>10^4$. We hypothesize that the two redox peak behavior for electron polaron formation peaks arises from contributions of the mixed side chain composition and the influence of mesoscopic domains of ordered (crystalline) and disordered (amorphous) aggregates in the polymer film.[31,32] It has been demonstrated that inter-chain electronic state hybridization can occur in ordered domains, which stabilizes the LUMO state (most positive reduction voltage) similar to the effect of charge-transfer hybridization, potentially resulting in a shift of the

observed reduction voltage between ordered and disordered domains.[33] Integration of the reduction current suggests ~50% of the film can be reduced to the bipolaronic state at 5 mV s^{-1} (corresponding to a charging time of 4 minutes), confirming fast charge transport through the bulk of the polymer electrode.[34]

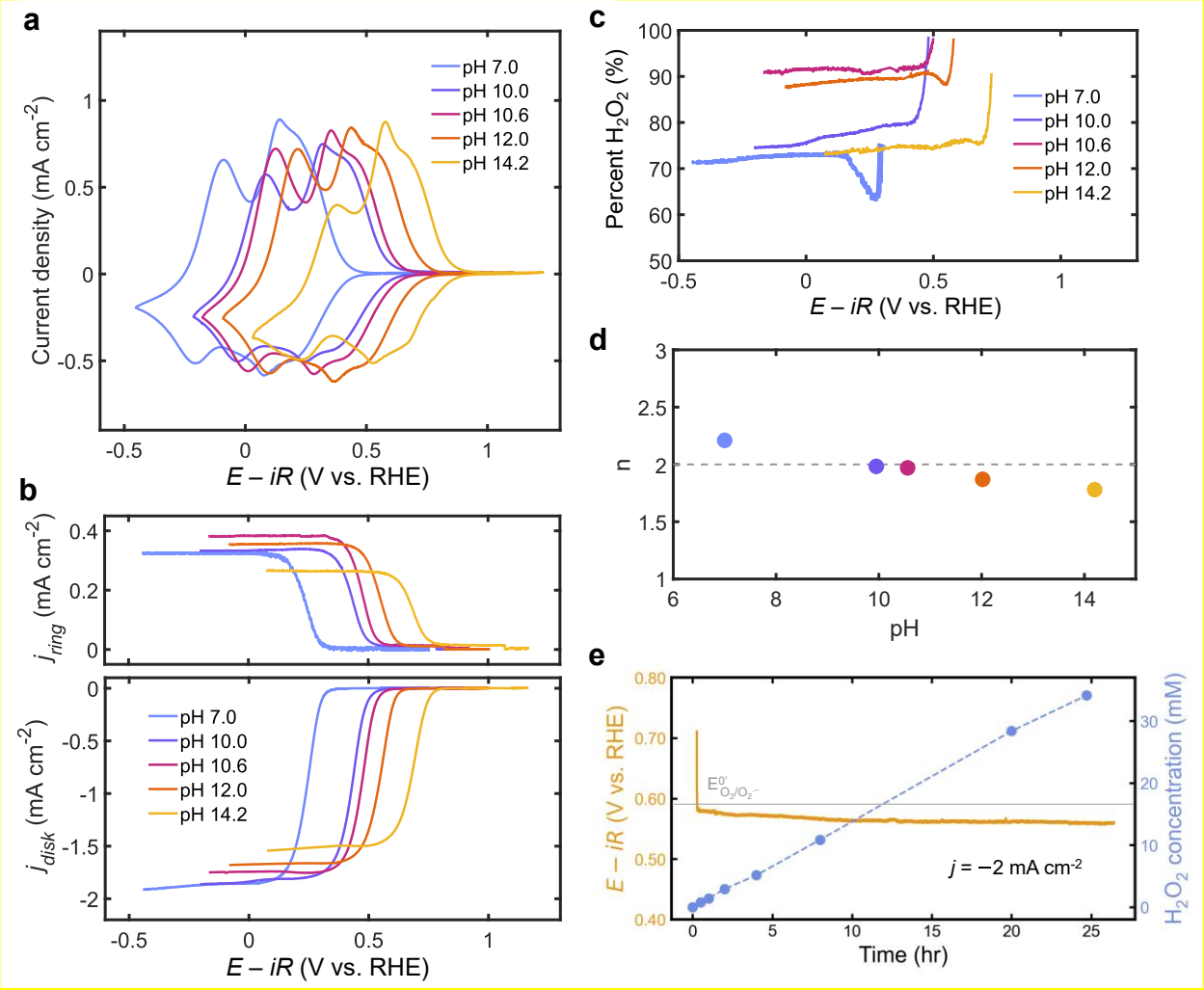

Figure 2. **a)** Ar-saturated reduction/oxidation voltammograms at a scan rate of 5 mV s^{-1}. **b)** O_2-saturated RRDE measurement at 1600 r.p.m. with a scan rate of 0.5 mV s^{-1}, showing a high ring current (E_{ring} = 1.20 V vs. RHE). **c)** Percent H_2O_2 produced calculated using the ring current from (b) and the electrode collection efficiency (N = 0.25). **d)** Number of electrons transferred during the ORR as calculated through Koutecký-Levich analysis. **e)** Quantification of H_2O_2 concentration obtained from constant current electrolysis (–2 mA cm^{-2}) in an H-cell performed on a carbon fiber paper supported p(NDI-T2 P75) film in 0.1 M KOH.

The oxygen reduction performance of p(NDI-T2 P75) as a function of electrolyte pH is presented in Figure 2b-d. In O_2-saturated electrolytes, we observe a large increase in current density at voltages correlated to the electron polaron redox reactions.

Interestingly, at constant pH, the limiting current density for oxygen reduction on p(NDI-T2 P75) remains constant regardless of polymer mass loading on the disk (Figure S4), suggesting that oxygen reduction is limited to the electrode/electrolyte interface. Additionally, the observed limiting current is half the limiting current of a polycrystalline Pt electrode (Figures S5-S7) tested in identical conditions. Assuming Pt reduces O_2 to H_2O through a net 4-electron process (as evidenced through the absence of ring-current and Koutecký-Levich analysis in Figure S6), the limiting current density measured for p(NDI-T2 P75) suggests the electrode is highly selective for the 2-electron product. High Faradaic efficiencies for H_2O_2 were additionally observed through collection on the ring electrode (Figures 2b, 2c) and Koutecký-Levich analysis (Figures 2d, S4). The polymer exhibited stable performance at –2 mA cm^{-2} for over 25 hours in a constant current electrolysis measurement performed in an H-cell (Figure 2e) with negligible changes in chemical composition observed through post-mortem XPS analysis (Figure S8). Similarly negligible changes were observed in the ^{1}H NMR chemical structure analysis of a sample tested for two hours in a constant voltage electrolysis measurement (Figure S9). SEM characterization of pristine and tested samples show similar morphologies, indicating no significant physical changes occur in the polymer after being tested for 25 hours (Figure S10). We observe a decrease in limiting current densities with increasing pH. In accordance with observations by McCreery et al., the pH-dependent variation of limiting current density suggests the reaction proceeds through a single-electron transfer reduction of dioxygen to superoxide followed by disproportionation of superoxide into hydro(gen) peroxide and dioxygen.[35] This is explained in detail in Section 9 of the Supplementary Information.

Comparing the trends in bulk redox and oxygen reduction, we observe an ~59 mV pH^{-1} positive shift in voltage versus RHE for both the electron polaron/bipolaron reactions and oxygen reduction (Figure S11). Although the overall ORR and HPPR are both proton-coupled, the observed pH-dependence reflects that both the bulk ion-insertion reactions and the rate-limiting step of oxygen reduction do not involve proton-coupled electron transfer. Instead, charge compensation for the electron polaron/bipolaron reaction is likely provided by K^+, the cation with majority concentration in these experiments.

O_2 Suppresses Electron Polaron Formation

To further study the reduction of oxygen to hydroperoxide on p(NDI-T2 P75), we monitor the electronic and chemical structure evolution of p(NDI-T2 P75) during operation through UV-Vis spectroelectrochemistry and *operando* Raman spectroscopy measurements.

The UV-Vis spectra of p(NDI-T2 P75) during reduction from its neutral to its bipolaron state in Ar-saturated 0.1 M KOH is presented in Figure 3a. The increase in optical density at ~500 nm and the respective decrease near 720 nm correspond to electron polaron formation, and the increase in optical density near 630 nm is indicative of the electron bipolaron state.[34] Figure 3b presents the differential optical density of the electron polaron feature at 500 nm with respect to time and voltage. The appearance and disappearance of the electron polaron feature in Ar-saturated electrolyte correspond well with the voltages observed in cyclic voltammetry. In O_2-saturated electrolytes, however, the intensity of the electron polaron feature was notably suppressed and shifted to more cathodic voltages. These results suggest the rate of O_2 reduction exceeds the rate of electron polaron formation in the film, where oxygen present in the electrolyte can rapidly consume the energetic electrons of the electron polaronic state of p(NDI-T2 P75) to generate hydro(gen) peroxide. Further evidence of this process is provided in Supplementary Figure S12 in which we track the polaron feature at 500 nm as the electrolyte feed to the spectroelectrochemical flow cell was switched repeatedly between Ar-saturated and O_2-saturated 0.1 M KCl electrolytes, resulting in the appearance and disappearance of the polaronic state, respectively.

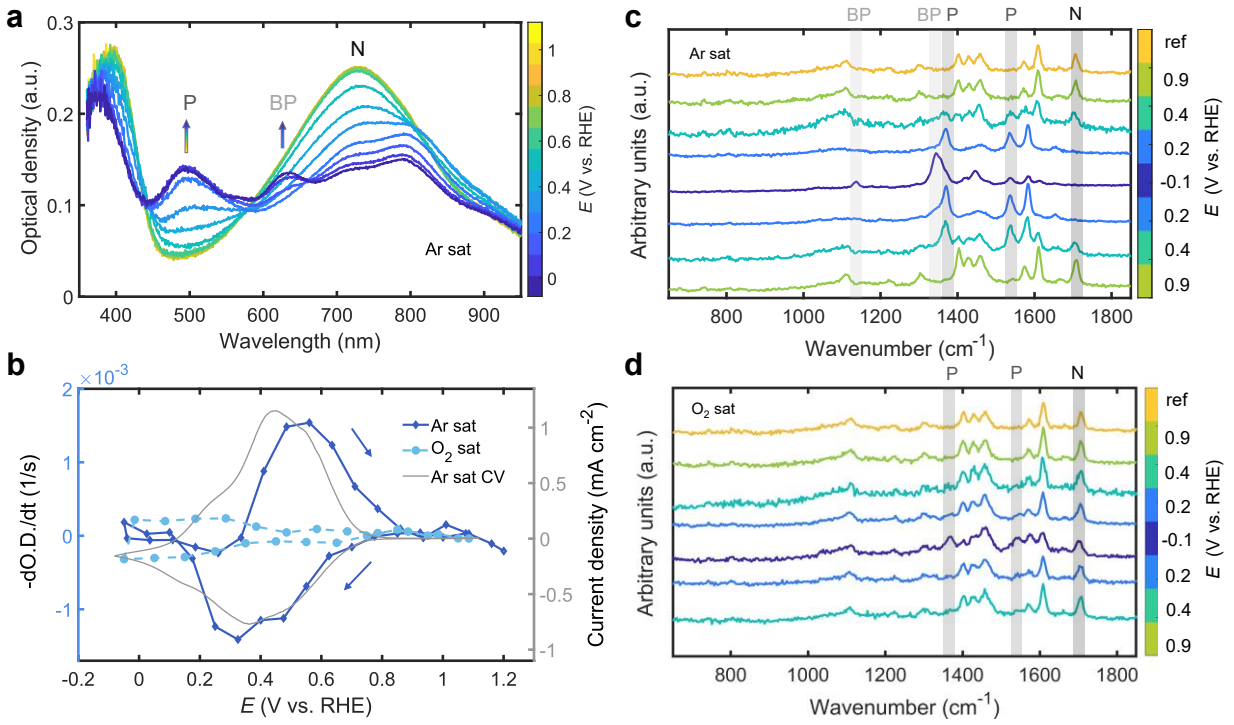

Figure 3. **a)** UV-Vis spectra of a thin p(NDI-T2 P75) film on indium tin oxide (ITO) glass as it is reduced in Ar-saturated 0.1 M KOH to its doubly-reduced, bipolaron state. Throughout the figure, dark grey (N), grey (P), and light grey (BP) labels are indicative of the neutral, electron

polaron, and electron bipolaron state of the polymer. **b)** Negative change in optical density at 500 nm with respect to time for Ar-saturated and O_2-saturated 0.1 M KOH as the polymer is reduced to its electron bipolaron state. The CV was collected in 0.1 M KOH at 5 mV s^{-1}. *Operando* Raman spectra for a thin p(NDI-T2 P75) film on ITO glass as it is reduced and oxidized in **c)** Ar-saturated 0.1 M KOH and **d)** O_2-saturated 0.1 M KOH.

Additional evidence that O_2 suppresses electron polaron formation in p(NDI-T2 P75) was obtained via *operando* Raman spectroscopy. We first describe the vibrational features of the neutral, polaronic, and bipolaronic states of the polymer measured at characteristic voltages in Ar-saturated electrolyte, shown in Figure 3c.

Starting with the initial reference spectrum obtained at the open-circuit voltage, the symmetric C=O stretching band at 1708 cm^{-1} can be used as an indicator for neutral repeat units as it has been shown to disappear as NDI-T2 becomes highly reduced.[36] As the applied voltage reaches 0.4 V vs. RHE and the material is reduced to its singly-reduced, electron polaron state, two new bands at 1538 and 1370 cm^{-1} arise. These bands can be ascribed to a shift of the pristine bands at 1610 and 1572 cm^{-1}, associated with the C-C stretching in the NDI unit. The intensities of these vibrations increase with applied voltage and are assigned to electron polaron formation.[36] Moreover, the intensity ratio of the triplet bands between 1496 and 1400 cm^{-1} undergoes a few changes, with a substantial drop of intensity of the bands at 1434 and 1406 cm^{-1}, assigned to collective vibrational displacements of the C-C stretching of the NDI and the T2 units. When the applied voltage reaches 0.2 V vs. RHE, the bands assigned to the electron polaron at 1583 cm^{-1} and 1370 cm^{-1} gain further intensity, while the triplet between 1496 and 1400 cm^{-1} broadens and loses intensity. Additionally, at this voltage, the band at 1708 cm^{-1}, which can be used to indicate the presence of neutral NDI-T2 repeat units, disappears. Once –0.1 V vs. RHE is applied, new vibrational features arise that have not previously been reported, namely the bands at 1344 and 1137 cm^{-1}, which, based on the associated electrochemical features, are likely associated with the formation of the electron bipolaron.

When similar measurements are performed in O_2-saturated electrolyte, we observe a suppression of the electron polaron features until the applied voltage reaches –0.1 V vs. RHE (in comparison to 0.4 and 0.2 V vs. RHE in Ar-saturated electrolyte). Additionally, bipolaronic vibrational bands are not observed in the presence of oxygen, and the neutral band in the Raman spectra does not disappear. These results confirm that electron polaron formation is suppressed through rapid consumption by O_2. Similar *operando* spectroscopic results are observed in 0.1 M KCl (Figure S13).

Oxygen Reduction on Metal-Free Electrodes

While our results reveal p(NDI-T2 P75) reacts directly with oxygen to form hydro(gen) peroxide, our *operando* spectroscopy results do not demonstrate evidence of a surface-bound intermediate expected for a catalytic, or inner-sphere, pathway. In this regard, we briefly describe the energetic contributions to ORR reactivity, highlighting the non-catalytic outer-sphere pathways for oxygen reduction which may occur at low overpotentials at high pH. Figure 4 presents a general, though not necessarily universal, framework to understand oxygen reduction to the 2-electron product in alkaline electrolytes (pH > 11.7) involving the commonly hypothesized surface adsorbate and solvated intermediates.[37–40]

(Electro)catalysis occurs through the adsorption of reaction intermediates (chemisorption/surface bond formation), which modulates their reduction potentials by $-\Delta G_{ads}/F$, where ΔG_{ads} is the Gibbs energy of adsorption and F is Faraday's constant.[41–43] In the "associative" pathway of the ORR, hypothesized to dominate on catalysts with single adsorption sites, the two O atoms remain bonded upon adsorption to theoretically yield *OOH through a net 2-electron/1-proton reduction. The adsorbed *OOH can then desorb to yield hydro(gen) peroxide (Figure 4) or be further reduced through a net 2-electron reaction to yield 2 molecules of H_2O or OH^-, depending on pH.

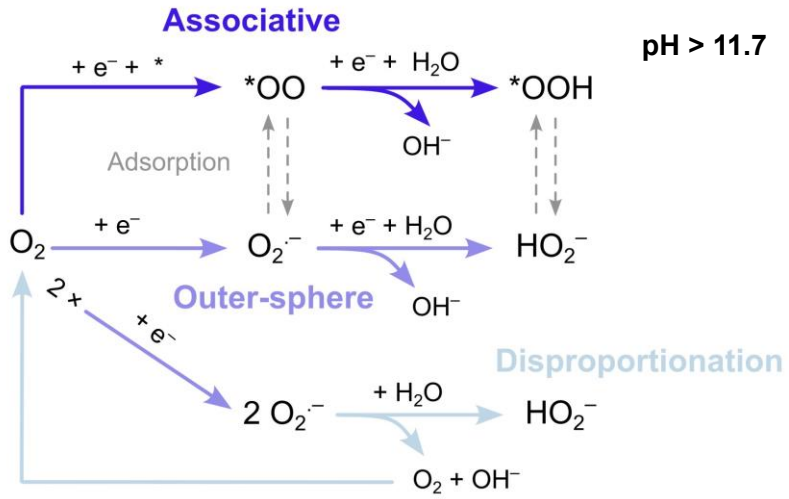

Figure 4. Reaction scheme for oxygen reduction to its 2-electron product in alkaline electrolytes. The * alone denotes a bare surface site, and *i represents a surface site with an adsorbed species i. The associative pathway is an inner-sphere reaction mechanism.

Alternative non-catalytic pathways for the 2-electron oxygen reduction, however, may occur without adsorption. In these outer-sphere pathways, the first electron transfer reaction to oxygen

is crucial. This initial reduction reaction is generally considered the rate-limiting step (RLS) due to its very negative standard reduction potential.[1,44,45] At pH > 4.88 (pK_a of HO_2), this step yields the superoxide radical, $O_2^{\cdot-}$, as shown in Reaction [1]:

$$O_2 + e^- \rightleftharpoons O_2^{\cdot-} \quad [1]$$

A detailed discussion on the standard and formal reduction potentials for this reaction ($E^0_{O_2/O_2^{\cdot-}}$ and $E^{0\prime}_{O_2/O_2^{\cdot-}}$, respectively) can be found in Supplementary Note 2.

In a fully outer-sphere reaction pathway, the second electron reduction yields hydrogen peroxide, H_2O_2, at pH ≤ pK_a = 11.7, or hydroperoxide, HO_2^-, at pH > pK_a and may proceed through the following reactions depending on pH:

$$O_2^{\cdot-} + H^+ + e^- \rightleftharpoons HO_2^- \qquad E^0_{O_2^{\cdot-}/HO_2^-} = 1.03 \text{ V vs. SHE} \quad [2]$$

$$O_2^{\cdot-} + 2H^+ + e^- \rightleftharpoons H_2O_2 \qquad E^0_{O_2^{\cdot-}/H_2O_2} = 1.72 \text{ V vs. SHE} \quad [3]$$

Beyond the inner-sphere “associative” and sequential outer-sphere electron transfer pathways, a pathway that accounts for the disproportionation of the unstable superoxide intermediate should also be considered (with x = 2 at pH < $pK_{a,H2O2}$; x = 1 at pH > $pK_{a,H2O2}$):

$$2\ O_2^{\cdot-} + x\ H_2O \rightleftharpoons O_2 + H_xO_2^{(x-2)} + x\ OH^- \quad [4]$$

Previous work has demonstrated that this reaction proceeds through a hydroperoxyl, HO_2, intermediate resulting in pH-dependent kinetics.[35] For the homogeneous disproportionation of radiolytically produced $O_2^{\cdot-}$, Bielski and Allen have determined an observed rate constant of k_{obsd} ($M^{-1}\ s^{-1}$) = $[7.61 \times 10^5 + 1.58 \times 10^{pH+3}][1 + 1.78 \times 10^{pH-5}]^{-2}$.[48] Because disproportionation generates both O_2 and H_2O_2 as a product, the O_2 can feed back into the electrochemical reaction cycle to generate additional current. Using this framework, McCreery et al. have demonstrated that the pH-dependence of oxygen reduction on glassy carbon electrodes proceeds through an outer-sphere 1-electron reduction to form superoxide followed by disproportionation.[35]

We summarize the energetics involved in the catalytic (inner-sphere) and non-catalytic (outer-sphere) pathways through a Pourbaix diagram (modified for the RHE scale) for the reactive oxygen species in Figure 5. When the ORR halfwave voltage ($E_{1/2}$) for oxygen reduction is

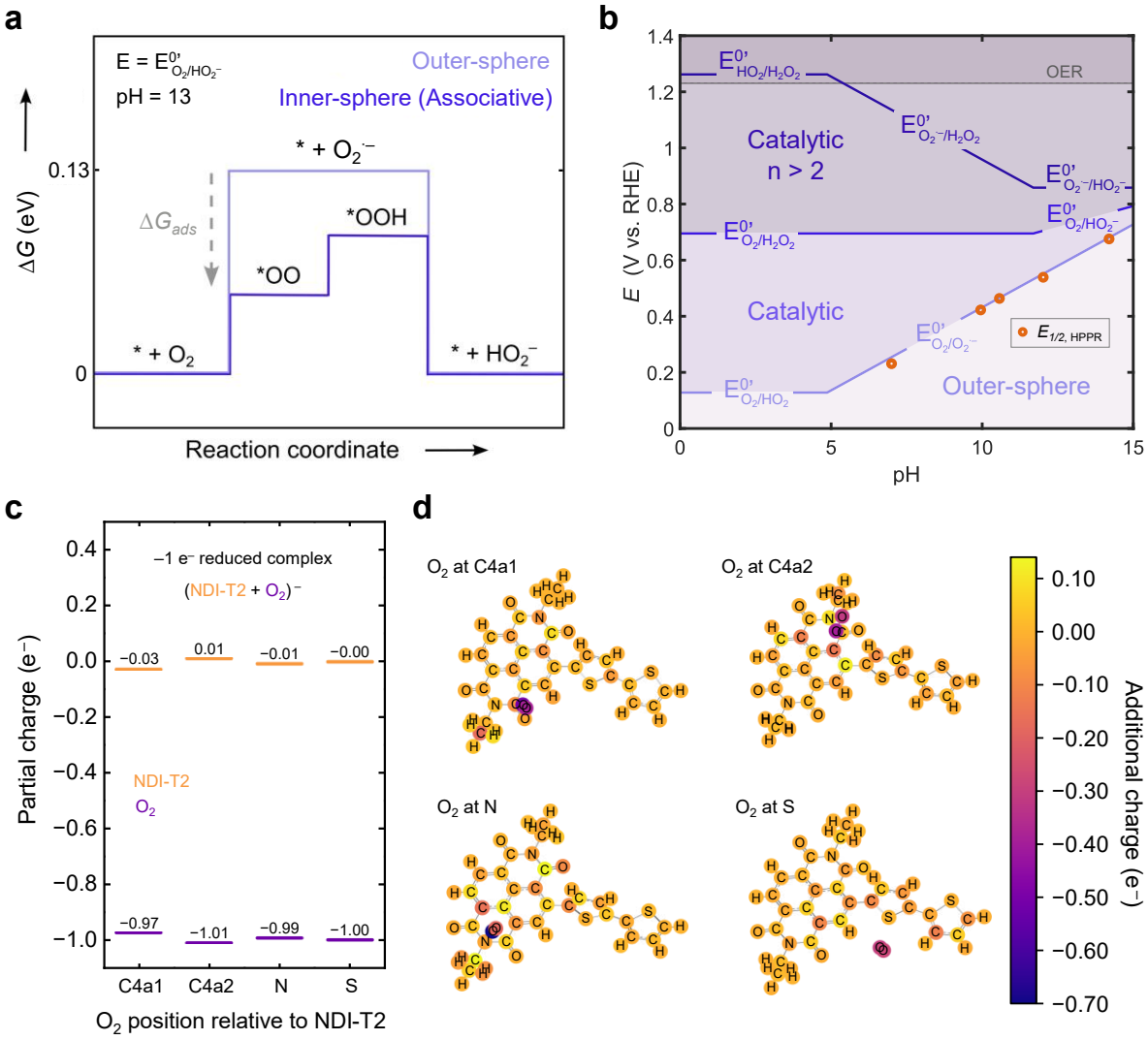

Figure 5. **a)** A qualitative comparison between the outer-sphere and inner-sphere reaction pathways. The adsorption energies are arbitrary but demonstrate how the formal reduction potentials are modified in a catalytic pathway. **b)** This modified Pourbaix diagram for the oxygen reduction reaction exhibits the pH-dependence of the formal reduction potentials of the single-electron reduction of O_2 ($E^{0\prime}_{O_2/O_2^{\bullet-}}$) and the two-electron reduction ($E^{0\prime}_{O_2/H_2O_2}$). The different regions of the diagram indicate roughly the voltages at which electrocatalysis occurs, depending on the observed $E_{1/2}$ of the ORR at different pH. The orange circles highlight the observed $E_{1/2}$ for oxygen reduction on p(NDI-T2 P75). **c)** The partial charges borne by the NDI-T2 monomer and O_2 for all four reduced $(\text{NDI-T2} + O_2)^-$ complexes in the singly reduced case. **d)** The additional charge ($Q_{add.} = Q_{red.} - Q_{neu.}$) distribution of the complexes with O_2 initiated 1.6 Å from the C4a1, C4a2, N, and S sites of NDI-T2.

positive of $E^{0\prime}_{O_2/H_2O_2}$ (or $E^{0\prime}_{O_2/HO_2^-}$), we assume the reaction proceeds through an inner-sphere catalytic pathway with at least partial selectivity for H_2O production. This means that the electron transfer number (n) in this regime will be greater than two because reducing O_2 to H_2O requires

four electrons. When the $E_{1/2}$ for oxygen reduction is below $E^{0\prime}_{O_2/H_2O_2}$ (or $E^{0\prime}_{O_2/HO_2^-}$) but above $E^{0\prime}_{O_2/O_2^{\cdot-}}$ (or $E^{0\prime}_{O_2/HO_2}$), the reduction of oxygen remains electrocatalytic but primarily results in H_2O_2. This is due to favorable adsorption of O_2, likely as *OO, which reduces the energy required to reduce O_2 to $O_2^{\cdot-}$ (Figure 5a). Conversely, if the $E_{1/2}$ for oxygen reduction is at $E^{0\prime}_{O_2/O_2^{\cdot-}}$ (or $E^{0\prime}_{O_2/HO_2}$), the initial reduction of oxygen to $O_2^{\cdot-}$ can be driven by an outer-sphere mechanism without the need for catalytic adsorption (see p(NDI-T2 P75) performance in Figure 5b). At $E_{1/2} < E^{0\prime}_{O_2/O_2^{\cdot-}}$ (or $E^{0\prime}_{O_2/HO_2}$), there are other factors limiting oxygen reduction, namely electronic conductivity. Still, in this case there is no requirement for catalytic adsorption and oxygen reduction may proceed through the outer-sphere mechanism.

The observed $E_{1/2}$ for oxygen reduction on p(NDI-T2 P75) occurs at $E^{0\prime}_{O_2/O_2^{\cdot-}}$ in all the pHs studied, strongly suggesting this reaction proceeds through an outer-sphere process limited by oxygen reduction to superoxide (Figure 5b, Figure S10). At the same time, our *operando* Raman and UV-Vis spectroscopy revealed that there is a direct chemical reaction between the polaronic state of the polymer and oxygen, forming a reduced oxygen species and re-oxidizing the polymer to the neutral state in the process (i.e. an electron transfer process mediated by the polymer). To rationalize these observations, we investigate the O_2 adsorption energetics of p(NDI-T2 P75) at different redox states and potential binding sites (Figure S14) using density functional theory (DFT). We consider the interactions of O_2 with the polymer in both the neutral and the 1 e^- reduced polaronic state by initializing the O_2 molecule 1.6 Å from the C4a1, C4a2, N, and S sites of NDI-T2, a similar distance to the C4a-O bond length in the C4a-hydroperoxyflavin complex, and comparing the calculated energies to a baseline case where O_2 is initialized far away.[49] A full description of the DFT calculation methods is provided in the Supplementary Information.

The neutral state of the polymer showed no affinity for binding O_2 (Figure S14). For the reduced states, the reduced complex (NDI-T2 + O_2)$^-$ and the case where isolated O_2 bears the entire negative charge are energetically identical and favorable relative to the case where the NDI-T2 alone bears the charge (Figure S15). We note here that the calculated energies deviate from expected experimental values and that this is likely due to the challenges in calculating the energy of O_2 molecules with DFT.[37] While this may affect the relative energy of the states with reduced O_2, it would not change the similarity of the energies of the reduced complex and the separated (NDI-T2) + (O_2^-) case, nor would it change the result that these two states are still the lowest energy states of the system.

Inspection of the partial charge distribution for the reduced complex (Figure 5c) shows that the extra –1 e^- charge is mainly localized on the O_2 molecule, leaving the NDI-T2 monomer almost neutral, irrespective of the O_2 location in the complex (Figure 5d). These results suggest that the lowest energy configuration is achieved when the added negative charge resides on O_2 and that the charged O_2 species (superoxide) is not stabilized by interaction with NDI-T2. Thus, although there is electron transfer between the reduced polymer and O_2 to form superoxide, it appears this process is chemical in nature and follows an outer-sphere process.

Outer-sphere Electron Transfer Followed by Disproportionation

Next, we explore the second electron transfer process. The reversible potential for superoxide reduction to hydro(gen) peroxide is positive of $E_{1/2} = E^{0\prime}_{O_2/O_2^{\cdot-}}$ for p(NDI-T2 P75) at all pHs explored in this study, suggesting superoxide formation is rate-limiting. If oxygen reduction on p(NDI-T2 P75) followed a serial 1+1 outer-sphere electron transfer pathway, we would expect a constant limiting current across the pH range (assuming that O_2 solubility remains approximately the same as suggested by the Pt ORR in similar electrolytes, Figures S5-S7). However, in addition to observing a pH dependence in the $E_{1/2}$ for oxygen reduction in the RRDE experiments, we observe a decrease in the limiting current density with increasing pH. This observation is unlikely to be due to surface roughness as the limiting current is not dependent on the mass of p(NDI-T2 P75) on the electrode (Figure S4). As demonstrated previously for metal-free carbon electrodes by Yang and McCreery,[35] this observation can be explained through disproportionation of the superoxide intermediate to form O_2 and hydro(gen) peroxide. The re-formed O_2 can then be electrochemically reduced to superoxide generating a limiting current density that falls between the expected values from the Levich equation for an n = 1 and n = 2 electron transfer reaction, depending on the disproportionation rate. The disproportionation rate has been observed to scale with the concentration of hydroperoxyl, HO_2, which decreases with increasing pH and thus lowers the observed limiting current density.[35,48]

We explore the possibility of disproportionation of superoxide following its formation from the outer-sphere reaction between the electron polaron in p(NDI-T2 P75) and oxygen through the use of a microkinetic simulation based on the following EC'D mechanism:

E: $N + e^- \rightleftharpoons P$ $E_1^{0\prime}$ [5]

C': $P + O_2 \rightleftharpoons N + O_2^{\cdot-}$ K_2 [6]

D: $2\ O_2^{\cdot-} + x\ H_2O \rightarrow O_2 + H_xO_2^{(x-2)} + x\ OH^-$ K_3 [7]

In this mechanism, the first electron transfer (E) converts the neutral polymer, *N*, into its reduced electron polaron state, *P*. The now electronically conductive polaronic state of the polymer can chemically reduce oxygen generating superoxide, $O_2^{\cdot-}$, while regenerating the neutral state of the polymer (C'). In the next step, superoxide radicals then disproportionate into O_2 and hydro(gen) peroxide (D) (Figure S16). We note that Step [6] corresponds to the elementary reaction considered in the DFT calculations.

A full description of the microkinetic model, solution procedure, and error analysis is included in the Supplementary Information. In short, reactions [5-7] are cast into a set of rate expressions, where k_i^* is an electrochemical rate coefficient (dependent on applied voltage), k_i is a chemical rate coefficient (independent of applied voltage), θ_N and θ_P, are the surface fractions of the polymer in its neutral and electron polaron states, respectively, and C_a^s is the concentration of species *a* at the surface of the electrode:

$$v_1 = k_{f,1}^* \theta_N - k_{b,1}^* \theta_P \quad [8]$$

$$v_2 = k_{f,2} \theta_P C_{O_2}^s - k_{b,2} C_{O_2^{\cdot-}}^s \theta_N \quad [9]$$

$$v_3 = k_{f,3} C_{O_2^{\cdot-}}^{s\ 2} \quad [10]$$

The fraction of the neutral and electron polaron states of the polymer as a function of applied voltage are determined using Butler-Volmer kinetics and the steady state approximation.[50,51] The steady state solutions are simultaneously fit to both the experimental log current density–voltage (or Tafel) data and the linear disk current density–voltage RRDE data at all pHs to extract a self-consistent set of fitting parameters describing the thermodynamics and kinetics of each elementary reaction step. The pH-independent fitting parameters are the formal reduction potential of reaction [5]: $E_1^{0\prime}$; and the associated chemical and electrochemical reaction rate coefficients and symmetry coefficients: k_1^0, β_1, $k_{f,2}$. The $k_{f,3}$ parameter is treated as pH-dependent, and each experimental pH has its own $k_{f,3}$ fit. Note that the equilibrium constant for reaction [6], K_2, is defined through $E_{O_2/O_2^{\cdot-}}^{0\prime}$ relative to $E_1^{0\prime}$, and K_3 is defined through the outer-sphere formal reduction potential of reactions [2-3] relative to $E_{O_2/O_2^{\cdot-}}^{0\prime}$.

The results of the simulation are shown in Figure 6, and the values of the fitting parameters are presented in Table 1. As is evident in Figure 6a and 6b, the simulation provides excellent fits of

the experimental data at all pH using a self-consistent set of fitting parameters and can explain the observed trends in pH-dependent limiting current and Tafel behavior across 4-orders of magnitude in kinetic current.

Table 1. Fitted parameters from the EC'D microkinetic simulation with their 95% Confidence Intervals.

Parameter	Value
$E_1^{0\prime}$ (V vs. SHE)	-0.3159 ± 0.0003
$\log k_1^0$ (mol cm^{-2} s^{-1})	-5.906 ± 0.002
β_1	0.4999 ± 0.0003
$\log k_{f,2}$ (cm s^{-1})	1.0807 ± 0.0004
$\log k_{f,3}^{pH=7}$ (cm^4 mol^{-1} s^{-1})	6.68 ± 0.03
$\log k_{f,3}^{pH=10}$ (cm^4 mol^{-1} s^{-1})	6.221 ± 0.004
$\log k_{f,3}^{pH=10.6}$ (cm^4 mol^{-1} s^{-1})	5.664 ± 0.002
$\log k_{f,3}^{pH=12.0}$ (cm^4 mol^{-1} s^{-1})	5.268 ± 0.005
$\log k_{f,3}^{pH=14.2}$ (cm^4 mol^{-1} s^{-1})	4.688 ± 0.005

The formation of the electron polaron in Step 1 of the reaction mechanism is identified as the RLS, which helps to explain the experimental observation of polaron suppression, whereby oxygen rapidly oxidizes any polaron formed through the chemical reaction in Step 2.[35]

In Figure 6c, the fitted $E_1^{0\prime}$ values are shown as dotted lines overlaying the experimental cyclic voltammograms of p(NDI-T2 P75) in Ar-saturated electrolytes. We find that the fitted $E_1^{0\prime}$ values show excellent agreement with the observed $E_{1/2}$ of the second polaron peak, which supports the hypothesized reaction EC'D mechanism. Finally, we look at the trend of $k_{f,3}$ with pH in Figure 6d. As expected, $\log k_{f,3}$ is linearly dependent on pH. However, in contrast to the observed slope of -1 by Bielski and Allen[48] for homogeneous disproportionation of radiolytically produced superoxide in free solution, we find a shallower decrease of –0.28 (R^2 = 0.95). The deviation from the expected slope may suggest that the p(NDI-T2 P75) can serve as a disproportionation catalyst for superoxide, although further work is needed to fully understand its origins.

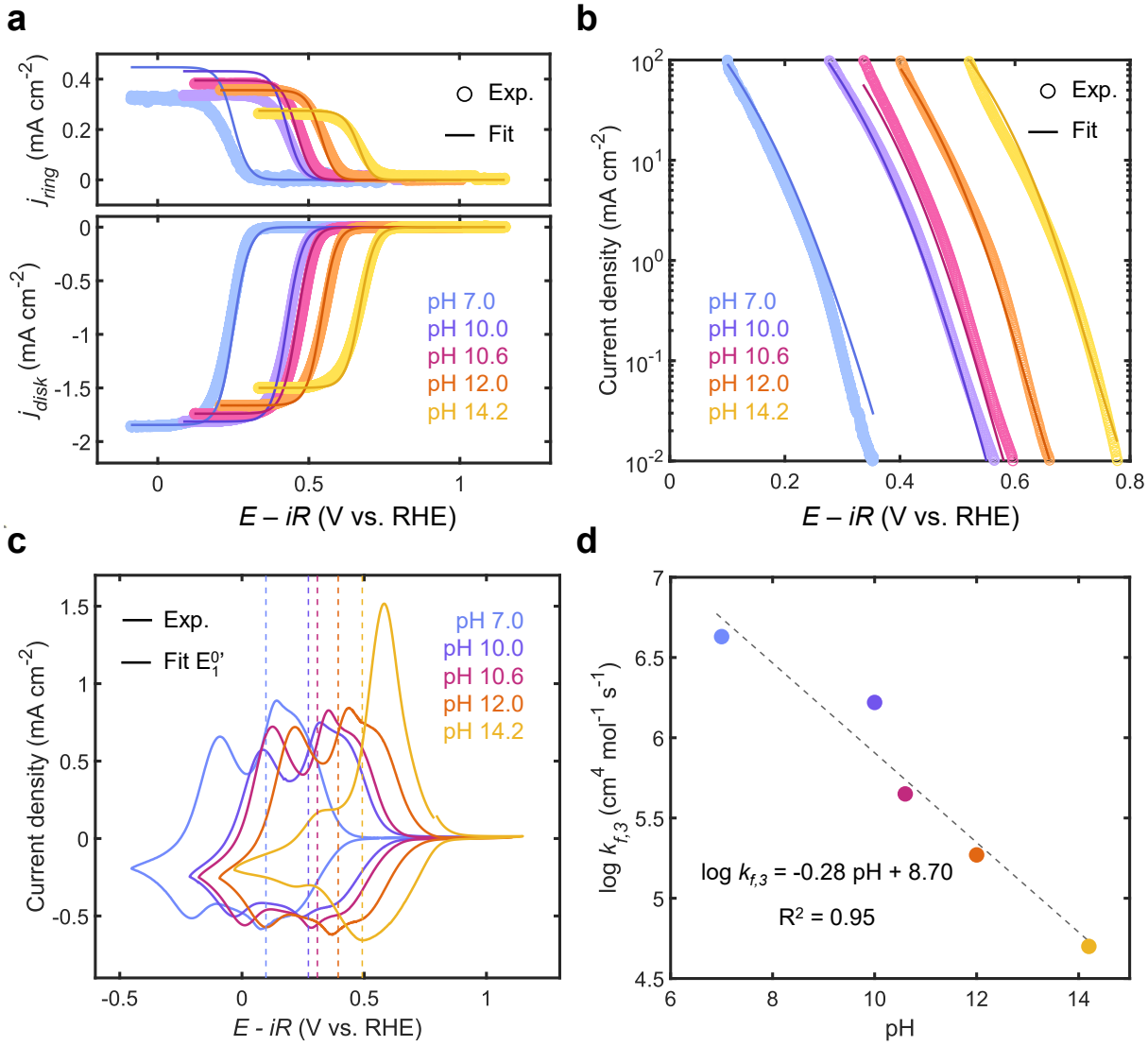

Figure 6. Results of the microkinetic simulation **a)** Experimental and simulated disk and ring current densities and **b)** kinetic current densities. **c)** Ar-saturated experimental cyclic voltammograms with overlay of fitted $E_1^{0\prime}$ value shown in the dashed lines. **d)** log $k_{f,3}$ versus pH observed in this work compared to results reported by Bielski and Allen,[48] showing the expected negative linear dependence but a shallower slope, suggesting the disproportionation process in this work is catalyzed.

Testing the Outer-sphere Hypothesis Using Other OMIECs

We further examine our proposed EC'D mechanism by benchmarking the oxygen reduction performance of select metal-free OMIECs as well as glassy carbon, which is the underlying substrate for these measurements and reduces oxygen through an outer-sphere pathway (Figure 7).[52] The polymers chosen were p(NDI-T)[53], p(gPyDPP-MeOT2)[54], and p(g3T2)[19] (Figure 7a).

First, we employ p(NDI-T)[53], which can be reduced to its electron polaronic state at voltages more positive than $E^{0\prime}_{O_2/O_2^{\cdot-}}$ (Figure 7b), to demonstrate that positively shifting the ion-insertion redox voltage does not shift the $E_{1/2}$ of oxygen reduction more positive than $E^{0\prime}_{O_2/O_2^{\cdot-}}$. In the EC'D process, when the voltage for the first electrochemical step (electron polaron formation) is positive of $E^{0\prime}_{O_2/O_2^{\cdot-}}$, the ORR will be thermodynamically limited by $E^{0\prime}_{O_2/O_2^{\cdot-}}$. Following this rationale, it is not surprising that p(NDI-T) and p(NDI-T2 P75) exhibit comparable HPPR activity (Figure 7c). Here, however, it is unclear whether polaron formation remains rate-limiting and the observed increase in current relative to p(NDI-T2 P75) may be due to a larger capacity of reactive electrons in the film or from a difference in electrochemically active surface area.

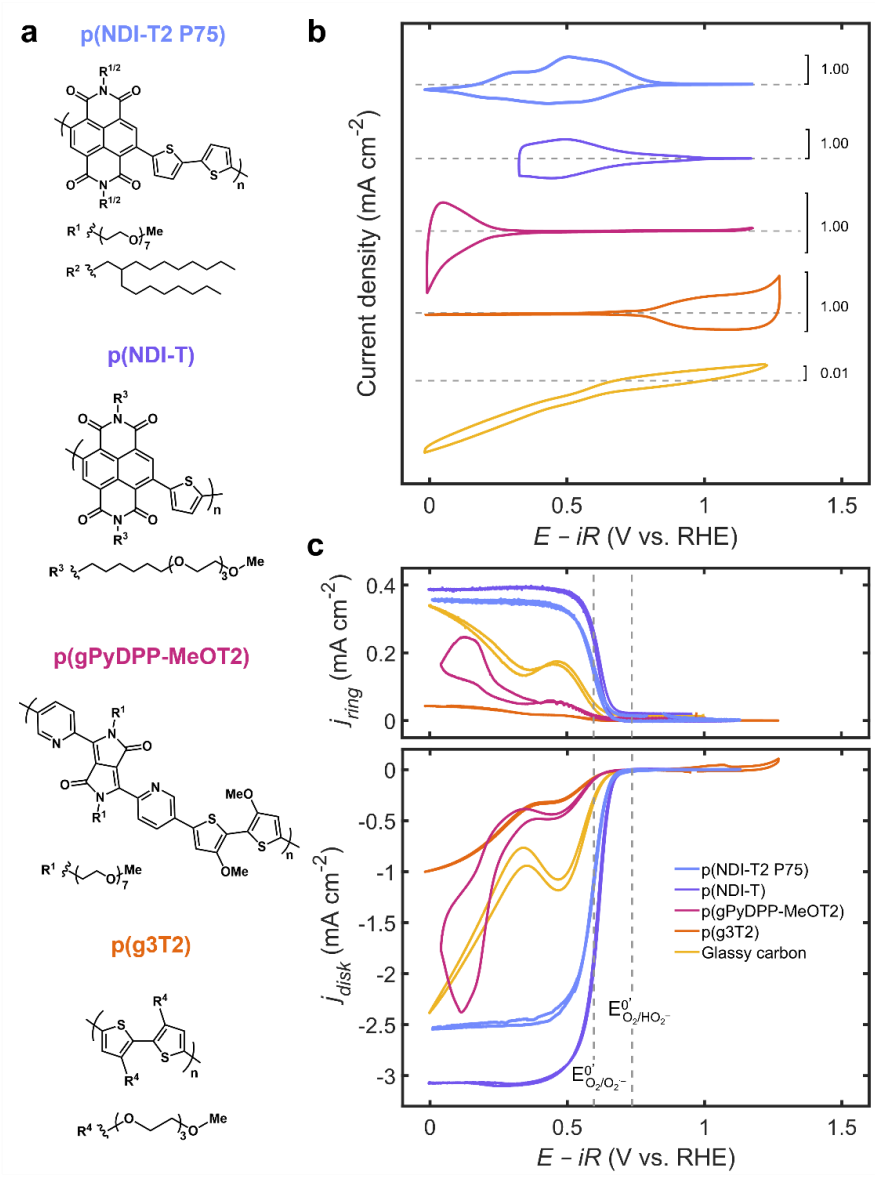

Figure 7. **a)** Chemical structures of the OMIECs tested, including p(NDI-T2 P75), p(NDI-T), p(gPyDPP-MeOT2) and p(g3T2). **b)** RDE measurements in Ar-saturated 0.1 M KOH at a scan rate of 5 mV s^{-1}. Current densities were scaled to highlight redox features. The voltammograms were scaled by a factor of 1, 1, 2, 2, and 50 for p(NDI-T2 P75), p(NDI-T), p(gPyDPP-MeOT2), p(g3T2), and glassy carbon, respectively. **c)** RRDE measurements in O_2-saturated 0.1 M KOH at 1600 r.p.m. at a scan rate of 0.5 mV s^{-1}.

Next, to assess the hypothesis that OMIECs first need to form the electron polaron and become electronically conductive before they can reduce oxygen, we evaluate p(gPyDPP-MeOT2), which has an electron polaron formation voltage more negative than $E^{0\prime}_{O_2/O_2^{\cdot-}}$ (Figure 7b). When the voltage for the electrochemical step is less than $E^{0\prime}_{O_2/O_2^{\cdot-}}$, the $E_{1/2}$ for oxygen reduction will correspond to the voltage of this first redox reaction, which is consistent with the proposed outer-sphere electron transfer for the initial reduction of O_2. Here, we take the $E_{1/2}$ for oxygen reduction to correspond to the largest increase in reduction current (~0.17 V vs. RHE), though we note the initial activity in p(gPyDPP-MeOT2) is attributed to the underlying glassy carbon substrate. In agreement with this finding regarding the crucial nature of the first electrochemical step, p(g3T2), a p-type OMIEC, does not effectively reduce oxygen through the EC'D mechanism with high activity because of the lack of ion-insertion redox at appropriate reduction voltages (Figure 7)—although here too there is likely some activity from the carbon substrate.

The effects of polaron formation voltage, $E_1^{0\prime}$, on oxygen reduction were additionally captured using the previously discussed microkinetic model (Figure S17a). As $E_1^{0\prime}$ shifts to negative voltages, the $E_{1/2}$ for oxygen reduction shifts negative accordingly. Inversely, for polaron formation voltage greater than p(NDI-T2 P75) ($E_1^{0\prime}$ > –0.31 V vs. SHE), the halfwave voltage for oxygen reduction is pinned by the outer-sphere formal reduction potential for the $O_2/O_2^{\cdot-}$ redox couple, $E^{0\prime}_{O_2/O_2^{\cdot-}}$, which then becomes the rate-limiting step in oxygen reduction. This explains the observation of the experimental shift in oxygen reduction current for n-type polymers with different polaron formation voltages and further supports the EC'D mechanism.

Figure S17b demonstrates that the disproportionation rate, $k_{f,3}$, primarily affects the limiting current densities but not the halfwave voltage of oxygen reduction, where low disproportionation rates result in only a single electron transfer (corresponding to exclusively superoxide formation) while high disproportionation rates push the electron transfer number towards n = 2 due to the feedback loop of generated O_2. Thus, the catalytic disproportionation of superoxide helps to rationalize the difference in observed oxygen reduction current between the p(NDI-T2 P75) coated electrode and the bare glassy carbon electrode—which shares the same $E_{1/2}$ but only generates half of the limiting current in 0.1 M KOH (Figure 7). On glassy carbon, which is

apparently less catalytic for superoxide disproportionation, the limiting current density corresponds to a single electron transfer to form superoxide which builds up at the electrode surface excluding O_2 resulting in a decrease in current density with increasing potential.[52,55]

While the side chains for the tested OMIECs are not identical, they all contain a polar (hydrophilic) portion, which is essential for bulk ion-insertion redox in aqueous electrolytes. In contrast, N2200, the NDI-T2 polymer with entirely nonpolar side chains, was found to be incapable of electrochemical activation and oxygen reduction in aqueous electrolytes (Figure S18). The OMIECs studied here span polymers with variations in backbone chemistry (homo- and co-polymers) and side chain chemistry, suggesting that the reactivity of many polymers within this class of materials may be rationalized through this EC'D mechanism when the terminal oxygen reduction product is hydro(gen) peroxide. However, we note our sample set of materials is still too narrow to make general claims across the whole range of OMIECs, and there are likely opportunities for alternative pathways that may even result in the 4-electron water product.[15]

Conclusions

In this work, we investigated a set of organic mixed ionic-electronic conducting polymers as single-phase electrodes for the oxygen reduction reaction, focusing on p(NDI-T2 P75) as a model system. In p(NDI-T2 P75), the halfwave voltages ($E_{1/2}$) for the bulk ion-insertion redox reactions (electron polaron formation) and oxygen reduction were found to be independent of pH, and the dominant product was found to be hydro(gen) peroxide (n = 2) across the pH range investigated. Despite the observed suppression of the polaronic state during oxygen reduction, the pH-dependent electrochemistry, *operando* UV-Vis and Raman spectroscopy, and DFT calculations did not provide evidence of a surface-bound intermediate. The reactivity was thus rationalized through an outer-sphere EC'D kinetic model, which extracted the polaron formation reaction as the rate-limiting step.

This interpretation explains the oxygen reduction reactivity trends of other mixed conducting polymers through the relationship between their polaron formation voltage and the outer-sphere formal reduction potential of oxygen to superoxide ($E^{0\prime}_{O_2/O_2^{\cdot-}}$). For polymers with $E_1^{0\prime} < E^{0\prime}_{O_2/O_2^{\cdot-}}$, the rate of oxygen reduction is limited by the rate of polymer reduction whereby the slower formed polaronic state is rapidly consumed (and thereby suppressed) by a chemical reaction with oxygen to form superoxide. Polymers with $E_1^{0\prime} > E^{0\prime}_{O_2/O_2^{\cdot-}}$ may bypass the chemical step, and the electrochemical oxygen reduction to superoxide then becomes rate-limiting. Additionally, this

interpretation explains the difference between the observed performance of the glassy carbon substrate and the mixed conducting polymers through the difference between their superoxide disproportionation rates, $k_{f,3}$. As seen on p(NDI-T2 P75), the catalytic disproportionation of superoxide leads to the same observed $E_{1/2}$ for oxygen reduction but results in almost twice the limiting current density.

While our results suggest the polymers in this study do not function as electrocatalysts for the initial reduction of oxygen to superoxide (i.e. through an adsorption-driven inner-sphere process), they suggest there may be opportunities for polymers to serve as catalysts for the disproportionation of superoxide into O_2 and $H_xO_2^{(2-x)}$. Additionally, the lack of metal centers that would likely drive intermediate adsorption enables p(NDI-T2 P75) to operate through the outer-sphere pathway and to be highly selective for H_2O_2 production at low overpotentials when operating in high pH, suggesting promising opportunities for this emerging class of polymer electrodes.

Experimental Methods/Materials

Materials

Polymers ActivInk® N2200 (P-0) was purchased from Flexterra and used without further purification. P75 was synthesized according to procedures previously described in the literature.[29] The polymers P75, p(NDI-T), p(gPyDPP-MeOT2), and p(g3T2) were purified by preparative Gel Permeation Chromatography (GPC, Japan Analytical Industry), using chloroform as the solvent. Paper electrodes (AvCarb P50T) were purchased from the FuelCellStore. 99.9 % potassium chloride (KCl) and 99.99% potassium hydroxide (KOH, semiconductor grade) were purchased from Sigma Aldrich. Argon (99.999%) and Oxygen (99.999%) gas were purchased from Praxair. Anhydrous chloroform was purchased from Sigma Aldrich. Potassium bicarbonate $KHCO_3$ (>99%) was purchased from Sigma Aldrich. Indium coated tin oxide (ITO) was purchased from Ossila.

Electrochemical characterization and RRDE measurements

Polymer solutions of p(NDI-T2 P75) were prepared by dissolving the polymer in chloroform at a mass concentration of 11.7 mg mL^{-1}. Prior to deposition, the RRDE was cleaned and polished with Al_2O_3 (particle size 0.05 μm) to a mirror finish. To create thick polymer films (estimated thickness = 1 μm), 10 μL of this solution was dropcast onto the glassy carbon disk of a rotating ring disk electrode (RRDE) (E6R1, Pt ring, polyether ether ketone (PEEK) shrouded, Pine Research) and the electrode was rotated at 400 r.p.m. for 2 min.

Three-electrode electrochemical measurements were conducted in an alkaline-resistant PTFE cell (AF01CKT1001, Pine Research Instrumentation) using a VSP-300 potentiostat (Biologic), with a leakless Ag/AgCl reference electrode (ET069, eDAQ), a coiled Pt wire counter electrode, and the RRDE with the dropcast or spin cast fims p(NDI-T2 P75) film. All voltages are referenced versus the reversible hydrogen electrode (RHE), where the RHE voltage of the Ag/AgCl reference for each experiment was standardized against a bulk RHE electrode (Hydroflex Hydrogen Reference Electrode, eDAQ) in each electrolyte prior to testing. The 0.1 M KOH electrolytes were prepared using KOH and ultrapure de-ionized water ("DI water", 18.2 MΩ resistance, MilliQ). The electrolytes for the pH series were made by mixing varying ratios of 1 M $KHCO_3$ and 1 M KOH stock solutions, where each stock solution was prepared in advance with ultrapure de-ionized water. Prior to electrochemical characterization, Ar gas was allowed to bubble through the solution for at least 30 minutes. For each experiment, the uncompensated resistance, *R*, was measured at open circuit voltage (polymer is in the pristine, neutral state) through electrochemical impedance spectroscopy (EIS) at the high frequency intercept and *iR* correction was completed manually during the data analysis phase. In the 1 M [K^+] electrolytes, The *R* values in the 1 M [K^+] 0.1 M [K^+] electrolytes were about 15 Ω and 58 Ω, respectively. In Ar-saturated solution, the Pt ring was electrochemically cleaned according to the procedure outlined by Chen et al.[56]

The p(NDI-T2 P75) film was then cycled five times between 0.2 V and –0.5 V vs. Ag/AgCl and another five times between 0.2 V and –1.0 V vs. Ag/AgCl at 5 mV s^{-1} scan rate. O_2 gas was then bubbled through solution for at least 30 minutes to saturate the electrolyte. In O_2-saturated solution, RRDE measurements were completed at different rotation rates (400, 900, 1200, and 1600 r.p.m., MSR Rotator, Pine Research) while the p(NDI-T2 P75) was cycled between 0.2 V and – 1.0 V at 5 mV s^{-1} and the ring was held constant at 1.2 V vs. RHE. At 1600 r.p.m., an extra RRDE measurement was completed following the same procedure as before, with a changed

scan rate of 0.5 mV s^{-1}. All the measured disk and ring currents were normalized by the disk electrode area (~0.196 cm^2).

H-cell measurements

Electrolysis was performed in a 2-compartment glass H-cell with a ceramic separator. The cathode compartment housed a 0.25 cm^2 Teflon-coated carbon paper (AVCarb P50T) electrode loaded with ~1 mg cm^{-2} polymer, and a leakless Ag/AgCl reference electrode (eDAQ). In the anode compartment, Ni foam (MTI) was used as the counter electrode, and each compartment was filled with 5 mL 0.1 M KOH. Electrolytes were stirred and O_2 was bubbled into the cathode test compartment throughout the experiment. At varying time intervals, 175 µL aliquots of sample were collected from the cathode compartment and replaced with fresh electrolyte.

Peroxide concentration was measured using a Cerium(IV) sulfate colorimetric assay.[28] Samples were prepared by mixing 175 µL of analyte, 700 µL of 1 mM Ce(IV) solution (in 0.5 M H_2SO_4), and 875 µL of 0.5 M H_2SO_4. The UV-visible spectrum (Cary 6000i UV-Vis Spectrometer) was recorded in transmission mode, and the intensity at 318 nm was used to quantify the Ce(IV) concentration in the sample, from which the H_2O_2 concentration was determined. A linear calibration curve was constructed by measuring analytes of known H_2O_2 concentration. When necessary, analytes were diluted in 0.5 M sulfuric acid to be within the measurement range of the assay.

Spectroelectrochemical measurements

Thin films on ITO coated glass substrates were prepared by spin coating. 65 µL of a p(NDI-T2 P75) solution (10 mg/mL) were spin coated onto a cleaned ITO coated glass substrates at 1000 r.p.m.. A thin layer of epoxy glue was applied at the edges of the film to prevent delamination (5 minute setting, Loctite Epoxy). The p(NDI-T2 P75) film was then placed into a quartz cuvette (DLC-300-Q-20, Starna Cells) filled with 0.1 M KOH. The electrochemical measurements were completed in a three-electrode set-up with a PEEK-shrouded leakless Ag/AgCl reference (eDAQ) and a coiled Pt wire as the counter. The UV-vis measurements were completed with a Tungsten light source (HL-2000-LL, Ocean Optics) and a spectrometer (QE Pro, Ocean Optics) and the instruments were synchronized using a Matlab code.[19]

Raman measurements

In-situ Raman spectra were acquired by a self-design electrochemical cell. (3D-printed by Protolabs, UK) with a miniature leakless Ag/AgCl reference electrode (eDAQ), and platinum sheet counter electrode (Sigma-Aldrich, USA). The samples were spin coated at 1000 r.p.m. for 60 s on an ITO slide (Kintec Inc, Hong Kong). Spectra were acquired in the Raman Stokes region using 532 nm excitation wavelength, in the range 150-2200 cm^{-1} (Horiba Xplora Confocal Raman). A 10x Olympus objective was used to perform measurements with laser power set at < 0.963 mW to avoid sample degradation. For a good signal-to-noise ratio, each spectrum was taken over an integration time of 20-30 s and averaged over three measurements. The spectrometer was calibrated through a Si sample using the spectral line 520.7 cm^{-1}. Spectra were analyzed using OMNIC software. Electrochemical signals were applied through a Bio-Logic potentiostat. A constant voltage was held for at least 30 seconds before each Raman measurement.

Microkinetic modeling

We use MATLAB R2019b to fit the model to the experimental data using the lsqcurvefit algorithm with MultiStart for 50,000 iterations.

The fitting parameters are the formal reduction potential to form the polaron (in the absence of O_2) in Step 1, $E_1^{0\prime}$, the polaron reaction's standard rate coefficient, k_1^0, and associated symmetry coefficient, β_1, the forward chemical rate coefficients of Step 2 (treated as pH-independent), and the pH-dependent forward rate constants of Step 3, $k_{f,3}^{pH=7}$, $k_{f,3}^{pH=10}$, $k_{f,3}^{pH=10.6}$, $k_{f,3}^{pH=12}$, $k_{f,3}^{pH=14.2}$.

The 95% confidence interval (*CI*) for each variable is calculated as (*q* = 21360 data points):

$$CI = \pm t_{\alpha=0.05,DOF=q-9}\, diag\left(\sqrt{S}\right) \quad [11]$$

The covariance matrix, *S*, is defined as:

$$S = R^2(A^TA)^{-1} \quad [12]$$

Where *A* is the Jacobian matrix of the fitted values with regards to the fitted coefficients, A^T is the transpose matrix of *A*, and R^2 is the mean square log error.

$$R = \frac{1}{q^{0.5}}\sqrt{\sum\left(\log j_{kinetic}^{model} - \log j_{kinetic}^{exp}\right)^2 + \sum\left(j_{RRDE,disk}^{model} - j_{RRDE,disk}^{exp}\right)^2} \quad [13]$$

The Jacobian matrix, *A*, is the partial derivative matrix of *j* with respect to the rate constants, i.e.:

$$A = \begin{bmatrix} \frac{\partial j_1}{\partial E_1^{0\prime}} & \cdots & \frac{\partial j_1}{\partial k_{f,3}^{pH=14.2}} \\ \vdots & \ddots & \vdots \\ \frac{\partial j_q}{\partial E_1^{0\prime}} & \cdots & \frac{\partial j_q}{\partial k_{f,3}^{pH=14.2}} \end{bmatrix} \quad [14]$$

Acknowledgements:

This work was supported by funding from Strategic Energy Research Consortium (SERC) of the Stanford Strategic Energy Alliance. A.F.D. acknowledges funding support from the Stanford Graduate Fellowship Program and the Ford Foundation Fellowship. H.Y. acknowledges funding support from the China Scholarship Council (CSC) through a Ph.D. studentship. J.N., D.P. acknowledge funding from the European Research Council (ERC) under the European Union's Horizon 2020 research and innovation program (grant agreement No. 742708, project CAPaCITy). Part of this work was performed at the Stanford Nano Shared Facilities (SNSF)/Stanford Nano-fabrication Facility (SNF), supported by the National Science Foundation under award ECCS-1542152.

Author contributions:

A.G. and J.T.M. conceived the idea. A.G., J.T.M, A.S., and W.C.C. supervised the work. A.F.D. performed the RRDE and UV-Vis spectroelectrochemistry characterization. A.F.D. performed the OECT measurements. A.Y.L. and I.D. performed the *operando* Raman measurements. H.Y., D.P., and J.N. performed the DFT calculations. A.F.D. and E.P. performed the H-cell peroxide quantification measurements. J.T. performed the XPS stability measurements. L.T. performed the NMR stability measurements. K.W. and A.M. performed the ICP-MS measurements. I.P.M., X.C., S.G., A.M., and A.G. performed the syntheses. J.T.M. developed the microkinetic simulation. All authors discussed the results and contributed to preparing the final draft of the manuscript.

Data availability

The experimental data that support the findings of this study are available via [Placeholder for data repository] (Ref. XX) (To be published simultaneously with the manuscript)

Conflicts of Interests:

There are no conflicts to declare.

Supplementary Information is available for this paper: Methods, Tables S1-S2, Figures S1-S15, Supplementary Discussion, and Supplementary References

*__Corresponding authors__: alexander.giovannitti@chalmers.se ; tmefford@stanford.edu

References

1 S. Vielstich, A. Lamm and H. Gasteiger, *Handbook of fuel cells. Fundamentals, technology, applications.*, United Kingdom, 2003.

2 K. Lee, O. Savadogo, A. Ishihara, S. Mitsushima, N. Kamiya and K. Ota, *J Electrochem Soc*, 2006, **153**, A20.

3 Y. Zuo, W. Sheng, W. Tao and Z. Li, *J Mater Sci Technol*, 2022, **114**, 29–41.

4 A. A. Gewirth and M. S. Thorum, *Inorg Chem*, 2010, **49**, 3557–3566.

5 C. Alegre, A. Stassi, E. Modica, C. lo Vecchio, A. S. Aricò and V. Baglio, *RSC Adv*, 2015, **5**, 25424–25427.

6 J. Ryu, M. Park and J. Cho, *Advanced Materials*, 2019, **31**, 1804784.

7 D. Yang, L. Zhang, X. Yan and X. Yao, *Small Methods*, 2017, **1**, 1700209.

8 Md. A. Rahman, X. Wang and C. Wen, *J Electrochem Soc*, 2013, **160**, A1759–A1771.

9 A. T. Murray, S. Voskian, M. Schreier, T. A. Hatton and Y. Surendranath, *Joule*, 2019, **3**, 2942–2954.

10 J. M. Campos-Martin, G. Blanco-Brieva and J. L. G. Fierro, *Angewandte Chemie International Edition*, 2006, **45**, 6962–6984.

11 S.-N. Zhang, Z.-H. Xue, X. Lin, Y.-X. Lin, H. Su, S.-I. Hirano, X.-H. Li and J.-S. Chen, *J Mater Chem A Mater*, 2020, **8**, 19793–19798.

12 B. Winther-Jensen, O. Winther-Jensen, M. Forsyth and D. C. MacFarlane, *Science (1979)*, 2005, **321**, 671–674.

13 P. D. Nayak, D. Ohayon, S. Wustoni and S. Inal, *Adv Mater Technol*, 2022, **7**, 2100277.

14 E. Mitraka, M. Gryszel, M. Vagin, M. J. Jafari, A. Singh, M. Warczak, M. Mitrakas, M. Berggren, T. Ederth, I. Zozoulenko, X. Crispin and E. D. Głowacki, *Adv Sustain Syst*, 2019, **3**, 1800110.

15 M. Vagin, V. Gueskine, E. Mitraka, S. Wang, A. Singh, I. Zozoulenko, M. Berggren, S. Fabiano and X. Crispin, *Adv Energy Mater*, 2021, **11**, 2002664.

16 B. D. Paulsen, K. Tybrandt, E. Stavrinidou and J. Rivnay, *Nat Mater*, 2020, 19, 13–26.

17 Y. Liang, Z. Tao and J. Chen, *Adv Energy Mater*, 2012, 2, 742–769.

18 Z. Zhang, W. Wang, X. Wang, L. Zhang, C. Cheng and X. Liu, *Chemical Engineering Journal*, 2022, **435**, 133872.

19 D. Moia, A. Giovannitti, A. A. Szumska, I. P. Maria, E. Rezasoltani, M. Sachs, M. Schnurr, P. R. F. Barnes, I. McCulloch and J. Nelson, *Energy Environ Sci*, 2019, **12**, 1349–1357.

20 J. Jang, J. Ha and J. Cho, *Advanced Materials*, 2007, **19**, 1772–1775.

21 J. Rivnay, S. Inal, A. Salleo, R. M. Owens, M. Berggren and G. G. Malliaras, *Nat Rev Mater*, 2018, 3.

22 K. Wijeratne, U. Ail, R. Brooke, M. Vagin, X. Liu, M. Fahlman and X. Crispin, *Proceedings of the National Academy of Sciences*, 2018, **115**, 11899–11904.

23 A. Giovannitti, C. B. Nielsen, D. T. Sbircea, S. Inal, M. Donahue, M. R. Niazi, D. A. Hanifi, A. Amassian, G. G. Malliaras, J. Rivnay and I. McCulloch, *Nat Commun*, 2016, 7.

24 V. Druet, P. D. Nayak, A. Koklu, D. Ohayon, A. Hama, X. Chen, M. Moser, I. McCulloch and S. Inal, *Adv Electron Mater*, 2022, 2200065.

25 Y. Sun, J. Wu, J. Tian, C. Jin and R. Yang, *Electrochim Acta*, 2015, **178**, 806–812.

26 S. K. Singh, K. Takeyasu and J. Nakamura, *Advanced Materials*, 2019, **31**, 1804297.

27 G.-F. Han, F. Li, W. Zou, M. Karamad, J.-P. Jeon, S.-W. Kim, S.-J. Kim, Y. Bu, Z. Fu, Y. Lu, S. Siahrostami and J.-B. Baek, *Nat Commun*, 2020, **11**, 2209.

28 Z. Lu, G. Chen, S. Siahrostami, Z. Chen, K. Liu, J. Xie, L. Liao, T. Wu, D. Lin, Y. Liu, T. F. Jaramillo, J. K. Nørskov and Y. Cui, *Nat Catal*, 2018, **1**, 156–162.

29 A. Giovannitti, I. P. Maria, D. Hanifi, M. J. Donahue, D. Bryant, K. J. Barth, B. E. Makdah, A. Savva, D. Moia, M. Zetek, P. R. F. Barnes, O. G. Reid, S. Inal, G. Rumbles, G. G. Malliaras, J. Nelson, J. Rivnay and I. McCulloch, *Chemistry of Materials*, 2018, **30**, 2945–2953.

30 T. Murata, K. Kotsuki, H. Murayama, R. Tsuji and Y. Morita, *Commun Chem*, 2019, **2**, 46.

31 D. Trefz, A. Ruff, R. Tkachov, M. Wieland, M. Goll, A. Kiriy and S. Ludwigs, *Journal of Physical Chemistry C*, 2015, **119**, 22760–22771.

32 R. Noriega, J. Rivnay, K. Vandewal, F. P. V. Koch, N. Stingelin, P. Smith, M. F. Toney and A. Salleo, *Nat Mater*, 2013, **12**, 1038–1044.

33 H. Meier, U. Stalmach and H. Kolshorn, *Acta Polymerica*, 1997, **48**, 379–384.

34 A. A. Szumska, I. P. Maria, L. Q. Flagg, A. Savva, J. Surgailis, B. D. Paulsen, D. Moia, X. Chen, S. Griggs, J. T. Mefford, R. B. Rashid, A. Marks, S. Inal, D. S. Ginger, A. Giovannitti and J. Nelson, *J Am Chem Soc*, 2021, **143**, 14795–14805.

35 H.-H. Yang and R. L. McCreery, *J Electrochem Soc*, 2000, **147**, 3420.

36 I. Denti, S. Cimò, L. Brambilla, A. Milani, C. Bertarelli, M. Tommasini and C. Castiglioni, *Chemistry of Materials*, 2019, **31**, 6726–6739.

37 I. C. Man, H. Su, F. Calle-Vallejo, H. A. Hansen, J. I. Martínez, N. G. Inoglu, J. Kitchin, T. F. Jaramillo, J. K. Nørskov and J. Rossmeisl, *ChemCatChem*, 2011, **3**, 1159–1165.

38 V. Viswanathan, H. A. Hansen, J. Rossmeisl and J. K. Nørskov, *ACS Catal*, 2012, **2**, 1654–1660.

39 J. B. Goodenough and B. L. Cushing, in *Handbook of Fuel Cells*, John Wiley & Sons, Ltd, Chichester, UK, 2010.

40 P. M. Wood, *Biochemical Journal*, 1988, **253**, 287–289.

41 A. J. Bard, *J Am Chem Soc*, 2010, **132**, 7559–7567.

42 N. Ramaswamy and S. Mukerjee, *Advances in Physical Chemistry*, 2012, **2012**, 1–17.

43 B. B. Blizanac, P. N. Ross and N. M. Markovic, *Electrochim Acta*, 2007, **52**, 2264–2271.

44 X. Ge, A. Sumboja, D. Wuu, T. An, B. Li, F. W. T. Goh, T. S. A. Hor, Y. Zong and Z. Liu, *ACS Catal*, 2015, **5**, 4643–4667.

45 A. Ignaczak, E. Santos and W. Schmickler, *Curr Opin Electrochem*, 2019, **14**, 180–185.

46 M. Schalenbach, *Int J Electrochem Sci*, 2018, 1173–1226.

47 W. H. Koppenol, D. M. Stanbury and P. L. Bounds, *Free Radic Biol Med*, 2010, **49**, 317–322.

48 B. H. J. Bielski and A. O. Allen, *J Phys Chem*, 1977, **81**, 1048–1050.

49 T. Wongnate, P. Surawatanawong, S. Visitsatthawong, J. Sucharitakul, N. S. Scrutton and P. Chaiyen, *J Am Chem Soc*, 2014, **136**, 241–253.

50 J. T. Mefford, A. A. Kurilovich, J. Saunders, W. G. Hardin, A. M. Abakumov, R. P. Forslund, A. Bonnefont, S. Dai, K. P. Johnston and K. J. Stevenson, *Physical Chemistry Chemical Physics*, 2019, **21**, 3327–3338.

51 J. T. Mefford, Z. Zhao, M. Bajdich and W. C. Chueh, *Energy Environ Sci*, 2020, **13**, 622–634.

52 J. R. Strobl, N. S. Georgescu and D. Scherson, *Electrochim Acta*, 2020, **335**, 135432.

53 A. Koklu, S. Wustoni, V.-E. Musteata, D. Ohayon, M. Moser, I. McCulloch, S. P. Nunes and S. Inal, *ACS Nano*, 2021, **15**, 8130–8141.

54 A. Giovannitti, R. B. Rashid, Q. Thiburce, B. D. Paulsen, C. Cendra, K. Thorley, D. Moia, J. T. Mefford, D. Hanifi, D. Weiyuan, M. Moser, A. Salleo, J. Nelson, I. McCulloch and J. Rivnay, *Advanced Materials*, 2020, **32**, 1908047.

55 V. F. Mattick, X. Jin, R. E. White and K. Huang, *J Electrochem Soc*, 2020, **167**, 124518.

56 S. Chen, W. Sheng, N. Yabuuchi, P. J. Ferreira, L. F. Allard and Y. Shao-Horn, *Journal of Physical Chemistry C*, 2009, **113**, 1109–1125.